Research Square

Preprints are preliminary reports that have not undergone peer review.
They should not be considered conclusive, used to inform clinical practice,
or referenced by the media as validated information.

Seashell-derived hydroxyapatite for selective interfacial adsorption of phospholipids from Antarctic krill oil

Tong Jiang
Ocean University of China
Meilin Zhang
Ocean University of China
Yihong Chen
Ocean University of China
Jian'an Sun
Ocean University of China
Yang Hu
huyang@ouc.edu.cn

Ocean University of China

Research Article

Keywords: Antarctic krill oil, hydroxyapatite, phospholipid enrichment, selective adsorption, solid-phase extraction

Posted Date: November 25th, 2026

DOI: https://doi.org/10.21203/rs.3.rs-11619543/v1

License: This work is licensed under a Creative Commons Attribution 4.0 International License.
Read Full License

Additional Declarations: No competing interests reported.

Seashell-derived hydroxyapatite for selective interfacial adsorption of phospholipids from Antarctic krill oil

Tong Jiang, [a, b, c], Meilin Zhang, [a, b, c], Yihong Chen, [a, b, c], Jian'an Sun, [a, b, c], Yang Hu [a, b, c *]

[a] State Key Laboratory of Marine Food Processing and Safety Control, College of Food Science and Engineering, Ocean University of China, Qingdao, 266404, PR China

[b] Qingdao Institute of Marine Bio-manufacturing Industry, Qingdao Key Laboratory of Green Manufacturing of Marine Bioproducts, Qingdao, 266071, PR China

[c] Key Laboratory of Biological Processing of Aquatic Products, China National Light Industry, Qingdao, 266404, PR China

* Corresponding author at: Qingdao Institute of Marine Bio-manufacturing Industry, College of Food Science and Engineering, Ocean University of China, Qingdao 266404, PR China.

E-mail address: huyang@ouc.edu.cn (Y. Hu)

ABSTRACT: Phospholipids (PLs) in Antarctic krill oil (AKO) are valuable marine-derived bioactive lipids with superior nutritional functions. However, selective separation of PLs was limited by the complex lipid composition of AKO and the lack of selective separation strategies. Herein, shell-derived hydroxyapatite nanoparticles (SHAP) were synthesized through microwave-assisted chemical synthesis, as a highly selective adsorbent for PLs enrichment from AKO. The obtained SHAP exhibited an adsorption capacity of 94.21±4.87 mg/g, 13.3 times that of triacylglycerols. The adsorption data fitted the Langmuir isotherm and pseudo-second-order kinetics, indicating the monolayer adsorption via synergistic physisorption and chemisorption. The selective enrichment was attributed to hydrogen bonding between the surface hydroxyl groups on SHAP and the polar headgroups of PLs, together with ligand exchange between phosphate groups and surface Ca^{2+} sites. To assess its practical applicability, SHAP was employed for the enrichment of PLs from AKO. Through simple adsorption, the PL purity was elevated from 34.90% in raw AKO to 91.16%. These results highlighted SHAP as a promising adsorbent for selective PLs enrichment, offering new opportunities for the high-value utilization of AKO.

KEYWORDS: Antarctic krill oil; hydroxyapatite; phospholipid enrichment; selective adsorption; solid-phase extraction

1. INTRODUCTION

Antarctic krill, a key component of the Southern Ocean ecosystem, is only 3–5 cm in length but represents the largest wildlife biomass on Earth (300–500 million tons) (Bar-On et al., 2018). The lipid content of Antarctic krill can exceed 40% of its dry mass, forming a substantial reservoir of fatty acids (Heyen et al., 2023). In recent years, Antarctic krill oil (AKO) has attracted increasing attention due to its distinctive composition, characterized by a high proportion of phospholipids (PLs), ranging from 56% to 81% (Phleger et al., 2002). Due to the distinct amphiphilic structure, PLs have been reported to exhibit diverse nutritional benefits associated with liver function, cognitive performance, visual health, and immune regulation (Cui et al., 2022). Moreover, the *sn*-1/2 positions of PLs derived from krill oil were occupied by eicosapentaenoic acid (EPA) and docosahexaenoic acid (DHA), resulting in enhanced bioavailability and functional efficacy, compared with PLs derived from soybeans, particularly in cognitive, behavioral, and emotional health applications (Yu et al., 2022). It was reported that purified PLs exhibited superior anti-inflammatory activity and a more positive effect on cardiovascular disease than raw ones (Zhou et al., 2021). Therefore, efficient enrichment of PLs was essential for the high-value development of AKO.

Solid-phase extraction (SPE) has emerged as a promising tool for lipid enrichment, owing to its operational simplicity and reduced solvent consumption (Ma et al., 2023). Rational selection of adsorbents tailored to specific lipid matrices allowed tunable separation performance, thereby enabling the efficient and selective PLs enrichment (Takeda et al., 2024; Wende et al., 2026). Several adsorbents have been reported to efficiently adsorb PLs (Calvano et al., 2009; Gu et al., 2025; Martínez Pérez-Cejuela et al., 2018; Shen et al., 2014). For example, MCM-41-based mesoporous silica materials could adsorb up to 0.57 mmol/g of PC by

virtue of their high specific surface area (> 1000 m^2/g). Liu et al. have reported that ten commercial resins exhibited the capability to adsorb phosphatidylcholine (PC), with the adsorption capacities ranging from 16.1 to 107.2 mg/g (Y. Liu et al., 2009). However, in addition to PLs, AKO contains approximately 19–44% triacylglycerol (TAG), greatly hindering selective PLs separation from raw AKO. Recently, metal-based affinity materials have been used to selectively purify PLs from raw oil. Wang et al. fabricated an affinity material (glass fabric@MOF-808) for the selective extraction of PLs from human milk through the Lewis acid-base interactions between zirconium and phosphates (M. Wang et al., 2023). However, the adsorbent showed poor adsorption capacity for PLs (3.31–6.54 mg/g). It remains challenging to selectively enrich PLs using an adsorbent with specific recognition and high adsorption capacity.

Hydroxyapatite (HAP, $Ca_{10}(PO_4)_6(OH)_2$) represents an attractive platform for PLs adsorption that can be prepared from biogenic sources such as shells, coral, bovine bones, and fish bones (S.-C. Wu et al., 2024). It typically possessed a hexagonal crystal structure, with positively charged Ca-sites and negatively charged P-sites on the crystal surface, serving as an adsorbent with bifunctional adsorption sites (Amenaghawon et al., 2022). This feature allowed adsorption through multiple mechanisms, including ion exchange, surface complexation, dissolution-reprecipitation, and electrostatic interactions. For PL, it possessed polar phosphate headgroups that may interact with the C-sites on HAP, whereas neutral TAG lacked phosphate moieties and exhibited negligible binding affinity. Such differences in intermolecular interactions rendered HAP a promising adsorbent for selectively enriching PLs from raw AKO.

Therefore, this study fabricated shell-derived hydroxyapatite nanoparticles (SHAP) through microwave synthesis for selective PL enrichment. The effects of synthesis parameters on PC adsorption were

systematically investigated, with PC as a model PL. Further, the specific affinity of SHAP for PLs in AKO was confirmed. Subsequently, the specific adsorption behavior and adsorption mechanism of PC on SHAP were demonstrated. Finally, the practical PLs enrichment performance of SHAP in AKO was optimized. The reported adsorbent provided a promising way for efficient PLs enrichment and high-value utilization of AKO.

2. MATERIALS AND METHODS

2.1. Reagents and samples

Natural shells were obtained from the beaches of Qingdao, China. Soybean lecithin (PC ≥ 90%) was purchased from Yuanye Bio-Technology Co., Ltd. (Shanghai, China). AKO was obtained Kangjing Marine Biotechnology Co., Ltd. (Shandong, China). $CHAP_1$ (used for protein separation), $CHAP_2$ (60–80 nm), $CHAP_3$ (acicular, 20 nm), titanium dioxide (TiO_2), and ammonium thiocyanate were purchased from Macklin Biochemical Co., Ltd. (Shanghai, China). Diammonium phosphate ($(NH_4)_2HPO_4$), ferric chloride hexahydrate ($FeCl_3 \cdot 6H_2O$), cyclohexane, chloroform, and isopropanol were procured from China Sinopharm Chemical Reagents Co., Ltd. All other chemicals were of analytical grade and purchased from commercial suppliers. Distilled water (18.2 $M\Omega \cdot cm^{-1}$) was obtained using a Millipore Milli-Q purification system.

2.2. Synthesis of SHAP

Following the method described by Pusparizkita et al. (Pusparizkita et al., 2025), calcined shell powder and phosphate were used as precursors for the microwave-assisted wet chemical synthesis of SHAP. Briefly, the shells were boiled in water for 30 minutes, rinsed with distilled water, and scrubbed carefully. The washed shells were dried in an oven at 80 °C to thoroughly remove moisture from their interior, after which they were ground and sieved through a 200-mesh sieve. The samples were heated in a muffle furnace to 850 °C at

10°C/min, followed by 2 h of calcination to obtain the calcium source. Upon calcination, the shell powder was dissolved in distilled water at room temperature and magnetically stirred to produce a suspension. Under a Ca/P feed ratio of 2.19, aqueous $(NH_4)_2HPO_4$ solution was added dropwise to the suspension to implement microwave-assisted synthesis. The mixture was magnetically stirred at 300 rpm for 30 minutes, after which the pH was adjusted to 11.5. Finally, SHAP was obtained through a 3-minute microwave treatment at a microwave power of 350 W. The material was then centrifuged, washed several times with water, and dried in an oven at 50°C for storage.

2.3. Adsorption-Desorption Experiment of PC

The adsorption experiment was adapted from Pinto et al. (Pinto et al., 2014). Soybean lecithin was dissolved in $CHCl_3$ at a concentration of 10 mg/mL. For the adsorption experiment, 30 mg of SHAP were added to 0.5 mL of the PC stock solution. After being shaken at 220 rpm and 20°C for 30 min in an incubator to complete adsorption, the suspension was centrifuged and the supernatant recovered. To eliminate surface-residual PC that might interfere with subsequent desorption experiments, the precipitate was washed twice using 1 mL of $CHCl_3$ each time. After washing, the PC was eluted with 0.5 mL of a ternary mixture consisting of $CHCl_3$/methanol/1M sodium phosphate, pH 7.2 (6/3/1, v/v/v). Desorption was carried out in a shaking incubator at 20°C and 220 rpm for 120 min, after which the mixture was centrifuged to recover the desorption solution. The determination of PC content was performed according to Stewart's protocol (Stewart, 1980). The typical adsorption capacity (Q_a), desorption capacity (Q_d), and desorption rate (D) were evaluated using Eqs. (1)–(3);

$$Q_a = \frac{(C_0 - C_a) \times V_a}{M} \quad (1)$$

$$Q_d = \frac{C_d \times V_d}{M} \quad (2)$$

$$D = \frac{Q_d}{Q_a} \times 100\% \quad (3)$$

where C_0 was the initial PC concentration (mg/mL), C_a referred to the PC concentration in the supernatant after adsorption (mg/mL), V_a represented the volume used in the adsorption experiment (mL), M was the mass of SHAP (g), C_d was the PC concentration in the desorption solution (mg/mL), and V_d was the volume of the desorption solution (mL).

2.4. Characterization

Fourier-transform infrared spectroscopy (FTIR) was used to identify characteristic functional groups of SHAP in the range of 4000–400 cm^{-1} using an iS50 FT-IR spectrometer (Thermo NICOLET). The crystal structure was determined by X-ray diffraction (XRD) (Rigaku MiniFlex 600, Japan) using Cu Kα radiation. The scanning range was 20–60° (2θ) with a step size of 0.02°. Scanning electron microscopy (SEM) images were obtained using a Sigma 500 scanning electron microscope (Zeiss, Germany). The specific surface area and pore size distribution were measured by a BET analyzer (Autosorb-iQ, Quantachrome, USA). Thermogravimetric analysis (TGA) was performed using a STA449F3 analyzer (NETZSCH, Germany) to analyze the changes in the adsorbent's mass over a temperature range of 30–800°C.

2.5. Investigation of Adsorption Properties

To evaluate the effect of the environmental solution on adsorption, 6 mg of SHAP were used to adsorb PC and TAG at an initial concentration of 0.3 mg/mL individually in different environmental solutions at a constant temperature of 20°C. Subsequently, static adsorption experiments were implemented to test the adsorption rate and maximum adsorption capacity of the SHAP adsorbent. For adsorption kinetic

measurement, supernatant PC contents were determined by sampling at predetermined time points of 2, 5, 10, 15, 20, 30, 45, 60, 90, 120, 180, and 240 min. For adsorption isotherm measurement, supernatant PC concentrations were detected after the adsorption system reached equilibrium under different initial PC concentrations. Further details regarding the kinetic and at equilibrium adsorption models were available in **Text S1**.

2.6. Adsorption studies on AKO

Adsorption experiments were conducted following the procedure described in Section 2.3. AKO was substituted for PC to investigate the adsorption behavior of SHAP in complex matrices. Then, the original AKO solution, supernatant, and eluate were collected for thin-layer chromatography (TLC) and high-performance liquid chromatography (HPLC) analysis. TLC was performed using TLC Silica gel GF_{254} plates from Qingdao Haiyang Chemical Co., Ltd. The developing solvent systems were petroleum ether/diethyl ether (8/2, v/v) and chloroform/methanol/water (65/25/4, v/v), respectively (D. Li et al., 2021). Visualization was achieved by fumigation with iodine vapor.

HPLC analysis of PLs and TAG was performed separately. TAG was analyzed by HPLC coupled with a refractive-index detector (RID; Shimadzu, Japan), using a Phenomenex Luna silica column (250 × 4.6 mm, 5 μm)(Gao et al., 2024). The column oven temperature was set to 30°C, and the mobile phase consisted of n-hexane/isopropanol/acetic acid (92:8:0.03, v/v/v) at a flow rate of 1 mL/min. PLs were analyzed by HPLC coupled with an evaporative light-scattering detector (ELSD; Waters, USA), using a YMC DIOL column (250 × 4.5 mm, 5 μm) (Han et al., 2019). The column oven temperature was set to 55°C, and the mobile phase consisted of buffer A (hexane/isopropanol/acetic acid/triethylamine, 81.42/17/1.5/0.08, v/v/v/v) and buffer B

(isopropanol/water/acetic acid/triethylamine, 84.42/14/1.5/0.08, v/v/v/v) at a flow rate of 1 mL/min. TAG contents in the adsorption experiments were quantitatively determined using an acetylacetone colorimetric method, as described in **Text S2**.

To achieve maximum enrichment of PLs from AKO, further optimization of the adsorption system was performed. A maximum SHAP dosage of 200 mg was applied, and adsorption assays were implemented on 500 μL of AKO matrix following the procedures in Section 2.3.

2.7. Statistical analysis

All measurements were performed in triplicate. The results were expressed as mean ± standard deviation (n = 3).

3. RESULTS AND DISCUSSION

3.1. Fabrication and Characterization of SHAP

In this study, SHAP were successfully fabricated via a microwave-assisted wet chemical route. Briefly, the calcined seashell was coprecipitated with phosphate ions in strongly alkaline environments under microwave irradiation, yielding HAP nanocrystals. To improve the PLs adsorption performance and reusability of SHAP, key preparation parameters were optimized with both Q_a and D values as indicators. **Fig. 1A** depicted the effect of calcium sources on the adsorption-desorption performance of the obtained SHAP toward PC. All the obtained HAP derived from $Ca(OH)_2$ (Chem), *Argopecten irradians* (Ai), *Scapharca subcrenata* (Ss), *Ruditapes philippinarum* (Rp), and *Neverita didyma* (Nd) exhibited a high Q_a value ranging from 110.95±3.90 to 120.45±2.37 mg/g, higher than that of reported resins 201×7 (107.2 mg/g)(Y. Liu et al., 2009). These high Q_a values were attributed to the high BET specific surface area of the

obtained HAP (**Table S1**), which provided abundant adsorption sites. Moreover, the suitable average pore sizes ranging from 18 to 22 nm (**Fig. S1**), which were reported to be suitable for PLs adsorption (D. Liu et al., 2018), were considered as another reason. It was observed that the D value of SHAP from Ai was significantly higher than those of other HAPs (80.91±2.17%). Therefore, Ai was selected as the calcium source for subsequent experiments.

The calcination temperature in HAP synthesis route was then optimized. As the calcination temperature increased to 850°C, the Q_a and D values of the resulting SHAP gradually increased and then leveled off (**Fig. 1B**). When calcination temperatures were above 850°C, HAP could form a well-crystallized structure (**Fig. S2**) and show stable Q_a and D values. At a low temperature of 800°C, the conversion of shell-derived $CaCO_3$ to CaO was incomplete, which resulted in insufficient crystallization of HAP, leading to poor Q_a and D. Considering the increased energy consumption at elevated temperatures, 850°C was selected as the appropriate calcination temperature.

As shown in **Fig. 1C**, the feed Ca/P molar ratio was also investigated over the range of 1.33 to 2.50. As the Ca/P ratio increased, the Q_a values rose significantly, while the D values decreased. This phenomenon was attributed to the changes in surface properties and crystal composition of HAP at different Ca/P ratio. As shown in **Fig. S3A**, the number of hydroxyl groups on the HAP surface decreased with increasing Ca/P ratio. The decrease in hydroxyl groups resulted in the exposure of calcium sites, enhancing the interaction of PLs with calcium sites on HAP surface (Bai et al., 2022), which led to an increase in Q_a, accompanied by a slightly decreased in D value. When the Ca/P ratio was further increased to 2.50, an undesirable $Ca(OH)_2$ phase was observed (**Fig. S3B**). $Ca(OH)_2$ could flocculate with PC (Cotmore et al., 1971), which markedly reduced the

D value. Therefore, a feed Ca/P ratio of 2.19 achieved the optimal balance between HAP crystal formation and the accessibility of surface adsorption sites. At this condition, HAP exhibited a Q_a of 111.67±1.43 mg/g and a D of 79.92±4.11%.

The initial pH value during the formation of HAP was another significant factor affecting the microstructural morphology and particle characteristics of HAP (Sadat-Shojai et al., 2023). **Fig. 1D** showed the effect of pH on the performance of HAP. As the pH increased from 9.0 to 11.5, Q_a increased from 56.55 ± 3.75 mg/g to a maximum of 128.51 ± 4.98 mg/g, while D decreased from 96.00 ± 4.24% to 80.73 ± 5.61%. At high pH values, a decrease in hydroxyl groups was observed on HAP (**Fig. S4**), which exposed the adsorption sites and therefore facilitated PC adsorption. This point was also considered as the reason for the decrease in D value. In this work, the pH value of 11.5 was chosen as the optimal pH value.

Microwave power was also considered as a key factor affecting the adsorption-desorption properties of SHAP. As shown in **Fig. 1E**, both the Q_a and D values gradually increased from 70 W to 350 W, then decreased at higher power levels. In the HAP formation process, increasing microwave power promoted uniform heating and facilitated the formation of HAP. However, excessively high microwave power may result in localized overheating due to excessive microwave energy, leading to unstable fluctuations in adsorption performance(Fitriyana et al., 2024). Therefore, 350 W was considered as the optimal microwave power. Based on these results, optimized SHAP were synthesized from Ai calcined at 850°C, with a Ca/P feed ratio of 2.19, a pH before microwave of 11.5, and a microwave power of 350 W, showing a Q_a value of 123.18±4.11 mg/g and a D value of 80.09±3.61%.

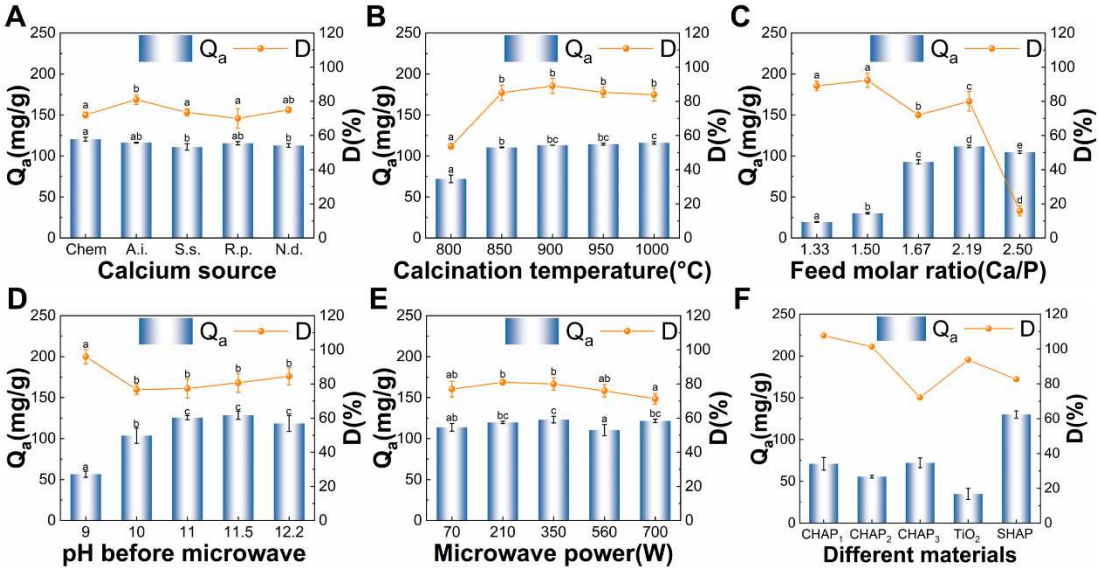

Fig. 1 Effects of preparation parameters on the adsorption desorption performance of HAP toward PC. (A) Calcium source: Chem, (chemically synthesized HAP); Ai, (*Argopecten irradians*); Ss, (*Scapharca subcrenata*); Rp, (*Ruditapes philippinarum*); Nd, (*Neverita didyma*). (B) Calcination temperature. (C) Feed molar ratio of Ca/P. (D) pH before microwave. (E) Microwave power. (F) Comparison of the adsorption-desorption properties among obtained SHAP, different commercial hydroxyapatite (CHAP) samples and TiO_2 adsorbent

Then, the adsorption performance of the obtained SHAP was compared with that of commercial CHAP samples (i.e., $CHAP_1$ used for protein, $CHAP_2$ with a particle size of 60-80 nm, and acicular $CHAP_3$ with a particle size of 20 nm) with similar size and TiO_2 particles that have been reported for the specific adsorption of PL. As shown in **Fig. 1F**, the synthesized SHAP exhibited a high Q_a value of 126.24±2.62 mg/g, higher than that of other materials, whose Q_a values ranged from 34.98±6.63 mg/g to 71.01±7.60 mg/g. This result demonstrated that SHAP held great promise as a PLs adsorbent, featuring high adsorption capacity and desorption rate suitable for practical adsorption applications.

Subsequently, the SHAP synthesized under the optimal conditions were systematically characterized. FTIR was first employed to characterize the functional groups on SHAP surface. As shown in **Fig. 2A**, the characteristic bands at 568, 601, and 1024 cm^{-1} corresponded to the ν_4 bending vibration and the ν_3

asymmetric stretching vibration of the phosphate ion, while the band around 3342 cm^{-1} corresponded to the OH group. All these are characteristic peaks of HAP. The weak peak at 1421 cm^{-1} corresponded to the ν_3 vibration of a small amount of carbonate substitution. This was caused by CO_2 in the air readily reacting with the strong alkali solution during the synthesis process, resulting in a small amount of CO_3^{2-} entering the HAP lattice and substituting for PO_4^{3-} (Type B substitution), which was a very common phenomenon in bio-derived minerals such as shells and bones (Nga et al., 2018). These FTIR results preliminarily showed the synthesis of hydroxyapatite.

XRD was utilized to further clarify the crystalline composition of the obtained SHAP. As shown in **Fig. 2B**, the XRD spectrum verified the crystalline structure of SHAP. The diffraction peaks at 2θ = 31.8°, 32.2°, 39.9°, 46.7°, and 49.5° were indexed to the (211), (112), (310), (222), and (213) crystal planes of HAP, respectively, which was consistent with the standard HAP diffraction pattern (JCPDS: 09-0432). A relatively large full width at half maximum was observed in the XRD pattern, which can be attributed to the particle size broadening effect associated with the nanocrystalline structure of SHAP, indicating its high surface reactivity (Frasnelli et al., 2017).

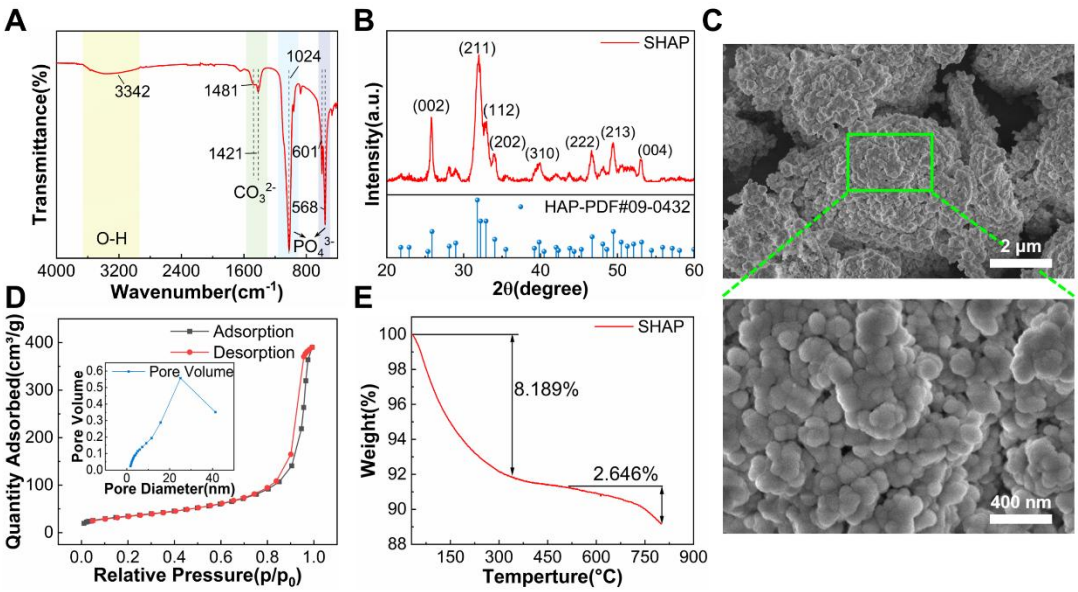

Fig. 2 Characterization results of the optimized SHAP: (A) FT-IR spectra; (B) XRD patterns; (C) SEM images; (D) N_2 adsorption-desorption isotherms and pore-size distribution (inset); (E) TGA curve

SEM was performed to characterize the microstructure and morphology of SHAP. As depicted in **Fig. 2C**, SHAP exhibited micrometer-scale agglomeration, showing a flower-seed-like granular structure, with individual particle sizes of approximately 125.7±28.4 nm. The uniform particle architecture was attributed to the microwave-assisted synthesis, promoting homogeneous nucleation and controlled particle formation, which was also observed in the microwave-assisted synthesis of mesoporous hydroxyapatite (J. Jiang et al., 2020). Then, the Ca/P ratio of the obtained SHAP was estimated according to energy-dispersive X-ray spectroscopy (EDX) analysis. As can be seen in **Fig. S5**, SHAP primarily consisted of C, O, Ca, and P, with a Ca/P ratio of 1.62. This value was close to the stoichiometric ratio of HAP (1.67). Trace amounts of Mg and Zn were also detected, which originated from naturally occurring mineral components in the shell precursor. The presence of microelements were also previously observed in other bio-derived HAP materials (Balabadra et al., 2024). The doping of Mg and Zn might be the reason for the superior performance of SHAP.

Pore structure governs the diffusion behavior and adsorption performance of porous materials. Therefore,

the structural properties of SHAP were further characterized by N_2 adsorption–desorption. As shown in **Fig. 2D**, the isotherm exhibited a Type IV profile with an H3 hysteresis loop at $P/P_0 > 0.4$, indicating the presence of slit-shaped mesopores generated by the aggregation of plate-like microspheres. The Brunauer-Emmett-Teller model was used to interpret the adsorption isotherms and calculate the specific surface area. The pore size distribution was determined using the BJH (Barrett-Joyner-Halenda) method. SHAP exhibited a specific surface area of 124.60 m^2/g, a pore volume of 0.61 cm^3/g, and an average pore diameter of 17.19 nm. These pore parameters demonstrated that SHAP possessed abundant mesoporous structures, which could facilitate mass transfer during PLs adsorption and resulted in the high adsorption capability.

Fig. 2E showed the TGA plot of the SHAP to assess the material's thermal stability. In the TGA curve, the first mass loss was observed above 100°C, primarily due to the volatilization of surface-adsorbed water (Mondal et al., 2019). The second rapid mass loss of 3–5% above 500°C was attributed to the Type B substitution decarboxylation process(D. Wang et al., 2025). Overall, the samples exhibited a total weight loss of approximately 10.82% at 800°C, confirming their good thermal stability.

Taken together, these characterizations confirmed the successful synthesis of SHAP with a mesoporous crystalline structure, abundant surface functional groups, and good thermal stability.

3.2. Capture PLs specifically in AKO using SHAP

The adsorption performance of SHAP was systematically investigated. Solvent environments could affect the surface tension of PC and TAG solutions, and the subsequent adsorption of PC and TAG on solid materials. In this work, methanol, ethanol, isopropanol, chloroform, n-hexane, and cyclohexane with different polarities were chosen as the solvents to investigate the adsorption performance of PC and TAG, with the aim

of confirming the selective adsorption of PLs on SHAP. The effect of solvent on adsorption was presented in **Fig. 3A**. In nonpolar solutions (i.e., chloroform, n-hexane, and cyclohexane), SHAP exhibited a higher adsorption capacity for PLs than that in polar solutions. Especially in cyclohexane, the adsorption capacities for PLs and TAG were 104.16±2.76 mg/g and 22.36±0.99 mg/g, respectively, giving the highest PLs/TAG adsorption ratio of 4.6 among all tested solvents. This result demonstrated that SHAP could act as an adsorbent for selectively purifying PLs from AKO. Therefore, the subsequent experiments were conducted with cyclohexane as the solvent.

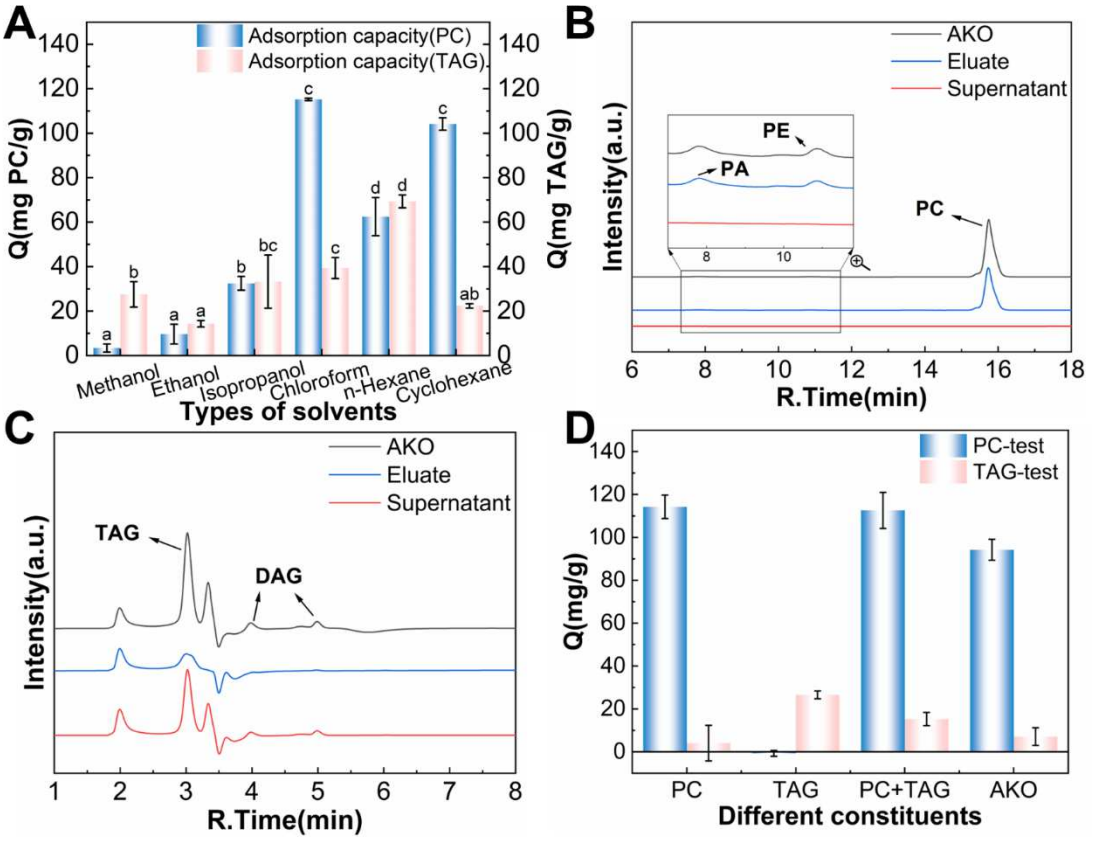

Fig. 3 (A) Adsorption performance of SHAP toward PC and TAG in various solvent systems. HPLC chromatograms of lipid fractions separated from AKO by SHAP: (B) PLs and (C) triacylglycerols during adsorption. (D) Adsorption capacity of SHAP toward PC and TAG in cyclohexane systems under different constituents

To evaluate the separation performance of SHAP toward AKO, TLC was used to analyze the lipid

compositions of AKO, the supernatant, and the eluate. As shown in **Fig. S6A**, PC, phosphatidylethanolamine (PE), TAG, and a small amount of lysophosphatidylcholine (LPC), which was likely generated through partial hydrolysis during long-term storage, were detected in the lane of AKO. After adsorption, intense TAG bands were observed in the supernatant, whereas PL bands were nearly absent, indicating negligible adsorption of TAG and almost complete removal of PLs from AKO. The eluate exhibited distinct bands corresponding to PC, PE, and LPC, confirming that the removed PLs were reversibly adsorbed on SHAP. The TLC results for TAG analysis (**Fig. S6B**) confirmed the absence of TAG in the eluate. Overall, these results demonstrated that SHAP could selectively adsorb PLs while leaving TAG in the supernatant, enabling the separation of PLs from AKO.

To further assess sample purity and separate potential analogous impurities, HPLC analysis was subsequently performed. **Fig. 3B** and **3C** show the PLs and glycerides composition of the AKO isolated by SHAP, obtained by HPLC-ELSD and HPLC-RID, respectively. Changes in PLs content were shown in **Fig. 3B**. According to the spectrogram of PLs standards, the peaks with a retention time of 7.5 min and 11 min corresponded to PA and PE. The peaks with retention times ranging from 15.5 to 16.1 min referred to PC. PA, PE, and PC were detected in AKO and the eluate, suggesting that SHAP could adsorb and desorb PLs. No PLs were detected in the supernatant, indicating that the PLs in AKO had been completely adsorbed. Changes in glyceride content were shown in **Fig. 3C**. The peak with a retention time of approximately 3 min corresponded to TAG, while the peaks at 4 and 5 min corresponded to DAG. Obvious peaks of TAG and DAG were observed in AKO and the supernatant, while only a weak TAG peak was found in the eluate, indicating that SHAP was capable of specifically separating PLs.

279 Furthermore, quantitative analysis of PC and TAG was conducted to elucidate the adsorption behavior
280 of SHAP in mixed lipid systems. As shown in **Fig. 3D**, using PC solution as the initial feed, an adsorption
281 capacity of 114.22 ± 5.45 mg/g for PC was obtained, with negligible TAG co-adsorption. Similarly, SHAP
282 exhibited an adsorption capacity of 26.53 ± 1.81 mg/g for TAG using TAG as the initial solution. For the PC-
283 TAG mixed system, the adsorption capacity of SHAP toward PC remained nearly unchanged (112.59 ± 8.41
284 mg/g), whereas the amount of adsorbed TAG decreased to 15.29 ± 3.07 mg/g, due to the specificity of SHAP
285 toward PLs. In the real AKO system, the PC/TAG adsorption ratio reached 13.3, higher than the
286 corresponding value of 7.4 in the PC-TAG system. This result indicated that SHAP still exhibited preferential
287 adsorption toward PC in a complex lipid mixture. Taken together, these results demonstrate that SHAP
288 exhibits a stronger affinity for PC than for TAG, enabling the selective separation of PLs from TAG in AKO
289 system.

290 **3.3. Behavior and Mechanism of PC Adsorption on SHAP**

291 The behavior and mechanism of PC adsorption on SHAP was systematically investigated. Adsorption
292 kinetic analysis was first conducted to clarify the rate-controlling step in the adsorption process. **Fig. 4A**
293 illustrated the kinetic model for the adsorption of PC on SHAP (C_0=0.15 mg/mL). In the first 20 minutes, the
294 adsorption amount increased rapidly, due to the presence of a large number of vacant active sites during the
295 early stages. Between 20 and 90 minutes, the adsorption rate slowed compared to the first stage. When the
296 adsorption time exceeded 90 minutes, the adsorption amount increased slowly and approached equilibrium
297 as the vacant active sites were gradually occupied until the system reached a dynamic equilibrium. Notably,
298 the adsorption reached equilibrium within approximately 90 min, demonstrating a relatively short equilibrium

time, which was favorable for practical lipid separation and industrial continuous-operation applications.

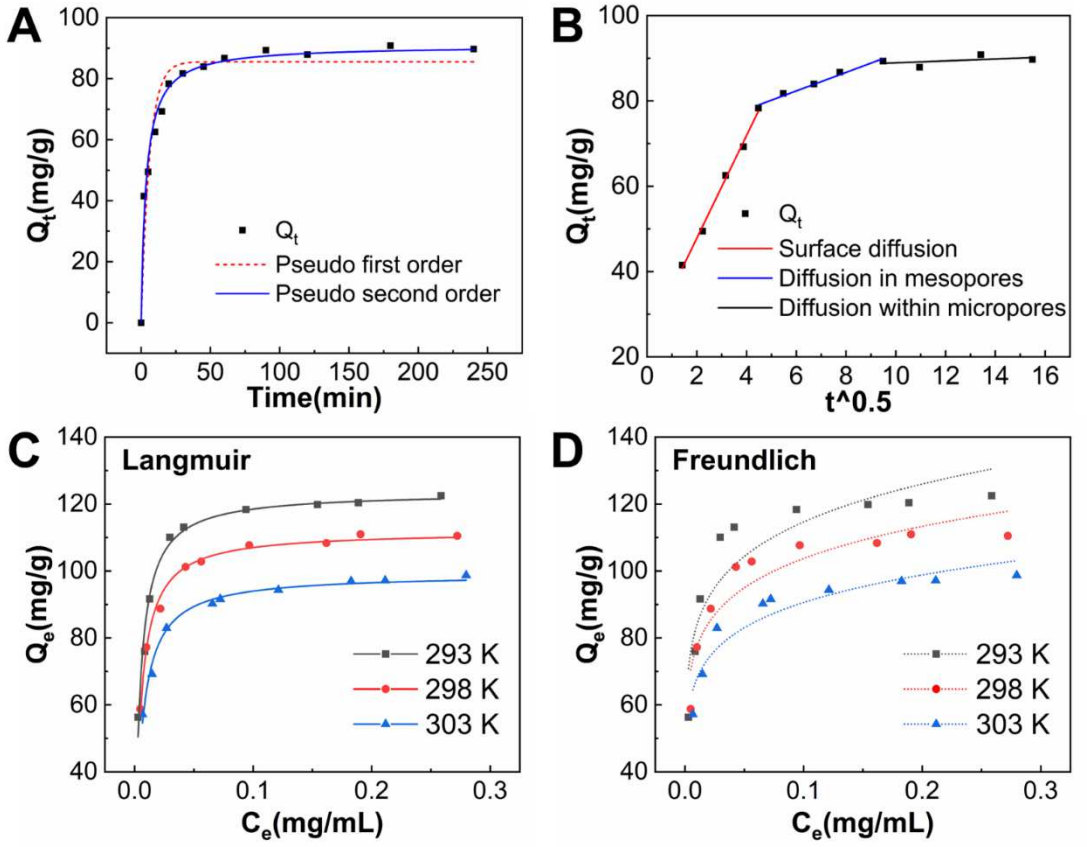

Fig. 4 Adsorption behavior of PC onto SHAP: (A) adsorption kinetic curves fitted by pseudo-first-order and pseudo-second-order models; (B) intra-particle diffusion model fitting plots; (C) Langmuir and (D) Freundlich isotherm fitting curves at 293 K, 298 K and 303 K

The adsorption kinetics curves were fitted using pseudo-first-order and pseudo-second-order kinetic equations. **Table 1** summarizes the calculated kinetic parameters and regression coefficients (R^2). The fitting results showed that the pseudo-second-order kinetic model could better describe the adsorption process, with a high R^2 value (>0.982). This means that there was a specific interaction between PC and SHAP, which can be used to explain the selective adsorption of PLs. The simulated Q_{sim} value of 90.89 mg/g was closer to the experimentally measured equilibrium adsorption capacity Q_{exp} of 90.85 mg/g. These results indicated that the adsorption of PC on the SHAP surface was not merely governed by physical interactions.

Table 1 The kinetic parameters and regression correlation coefficients (R^2)

Pseudo-first-order			Pseudo-second-order		
Q_{sim} (mg/g)	K_1 (min^{-1})	R^2	Q_{sim} (mg/g)	K_2 ($g \cdot mg^{-1}min^{-1}$)	R^2
85.57	0.165	0.931	90.89	0.003	0.982

The intraparticle diffusion model analysis was presented in **Fig. 4B**. The adsorption of PC onto SHAP followed a typical multi-stage mass transfer process. None of the fitted lines crossed the origin, revealing that intraparticle diffusion was not the sole rate-limiting step (Zhu et al., 2022). The steep slope of the first stage corresponded to film diffusion, where PC molecules diffused from the bulk solution through the liquid boundary layer to the outer surface of SHAP with low mass-transfer resistance. The markedly reduced slope in the second stage represented PC diffusion into the mesoporous channels of SHAP. Mass-transfer resistance rose with confined pore space, and mesoporous intraparticle diffusion became the dominant rate-controlling step (X. Jiang et al., 2024). In the third stage, the slope approached zero, corresponding to micropore diffusion and eventual adsorption equilibrium as internal active sites were gradually occupied (Lu et al., 2026). In summary, while external film diffusion contributed to the initial rapid adsorption, mesoporous intraparticle diffusion was the key rate-limiting step for PC adsorption on SHAP.

Then, the equilibrium adsorption isotherm was tested and fitted to the Langmuir and Freundlich models, as exhibited in **Fig. 4C** and **Fig. 4D**. The obtained fitting parameters and corresponding R^2 values were presented in **Table 2**. It can be seen that the equilibrium adsorption data exhibited a better fit to the Langmuir

model (R^2 higher than 0.977) than to the Freundlich model (R^2 lower than 0.887), indicating that PC adsorption on SHAP proceeded via monolayer coverage on energetically homogeneous adsorption sites (Zou et al., 2025). The Q_{max} values were also determined at different temperatures. As shown in Table 2, the Q_{max} value was maximum at 20°C (123.50 mg/g) and decreased with increasing temperature, suggesting that PC adsorption was an exothermic process and that PC-SHAP interactions could be promoted at low temperatures. The temperature-dependent variation of the Langmuir constant (K_L), which reflected adsorption affinity (Janusz & Skwarek, 2022), also confirmed this point.

Table 2 Isotherm model parameters for PC adsorption onto SHAP at different temperatures

Temperature (K)	Langmuir			Freundlich		
	Q_{max} (mg/g)	K_L (mL/mg)	R^2	n	K_F [(mg/g) · (mL · mg)$^{1/n}$]	R^2
293	123.50	236.31	0.977	7.35	156.80	0.823
298	111.91	217.64	0.991	7.87	139.09	0.852
303	99.11	183.21	0.985	7.93	120.95	0.887

The K_L values were further fitted to the Van't Hoff equation to determine the thermodynamic parameters (**Table 3**). The negative ΔG values demonstrated the spontaneous and thermodynamically feasible adsorption of PLs onto SHAP, while the negative ΔS suggested a more ordered arrangement of adsorbed PC molecules on the SHAP surface (Manyepedza et al., 2025). Furthermore, the standard enthalpy change ΔH was −31.17 kJ/mol, confirming the exothermic nature of the adsorption. Generally, this ΔH value indicated synergistic physisorption and chemisorption (Alamdari & Journey, 2026), which was consistent with the pseudo-second-order kinetic behavior and the specific interaction responsible for the selective adsorption of PC on SHAP.

Table 3 Fitting parameters of thermodynamics for PC adsorption onto SHAP

Adsorbents	ΔG (kJ·Mol^{-1})			ΔH (kJ·Mol^{-1})	ΔS (J·Mol^{-1}·K^{-1})
	293K	298K	303K		
SHAP	-29.4	-29.6	-29.3	-31.2	-5.8

To uncover the underlying adsorption mechanism, multiple characterizations were further carried out to analyze the structural and surface chemical variations of samples before and after adsorption. The specific surface area, pore volume, and average pore diameter of SHAP after adsorption were also determined (**Fig. 5A**). After adsorption, the specific surface area decreased significantly from 124.60 m^2/g to 59.17 m^2/g, the pore volume decreased from 0.61 cm^3/g to 0.39 cm^3/g, and the average pore diameter increased from 17.19 nm to 19.42 nm. The significant decrease in specific surface area and pore volume indicated that PC molecules were adsorbed onto the SHAP surface and partially blocked the pores, while the increase in average pore diameter was attributed to the preferential blocking of small pores, shifting the accessible pore size distribution toward larger diameters. Then, XRD analysis was used to determine the crystalline phase of SHAP after adsorption (**Fig. 5B**). Comparison of the results with standard JCPDS patterns revealed that all characteristic peaks of HAP were retained, indicating that adsorption occurred only on the surface, without disrupting the crystalline structure of SHAP or leading to the formation of new crystalline phases.

FTIR analysis of PC, SHAP, and SHAP after adsorption were carried out to detect the potential interaction between PC and SHAP during adsorption. As presented in **Fig. 5C**, the PC spectrum exhibited characteristic lipid-related absorption bands, including the stretching vibration of =C-H at 3010 cm^{-1}, the

asymmetric and symmetric stretching vibrations of C-H at 2920 cm^{-1} and 2849 cm^{-1}, and other lipid-related signals at 1735 cm^{-1} (C=O)(Y. Li & Liu, 2024; L. N. Y. Wu et al., 2009), respectively. Additionally, the characteristic peak of trimethylamine cations at 970 cm^{-1} was indicative of PC. The peak at 720 cm^{-1} arose from the out-of-plane wagging vibration of cis-HC=CH-$(CH_2)_n$ (Delfanian & Azizi, 2026). The characteristic peaks of HAP corresponding to P-O was observed at 1013 cm^{-1} in the spectrum of SHAP. The characteristic absorption peaks of unsaturated double bonds (3010 cm^{-1}) were clearly observed in the spectrum of SHAP after adsorption, confirming the successful loading of PC onto SHAP. Moreover, the stretching vibration of the P-O bond was strengthened, accompanied by a red shift, demonstrating intermolecular interactions between PC and the SHAP surface during adsorption (Gudyka et al., 2024).

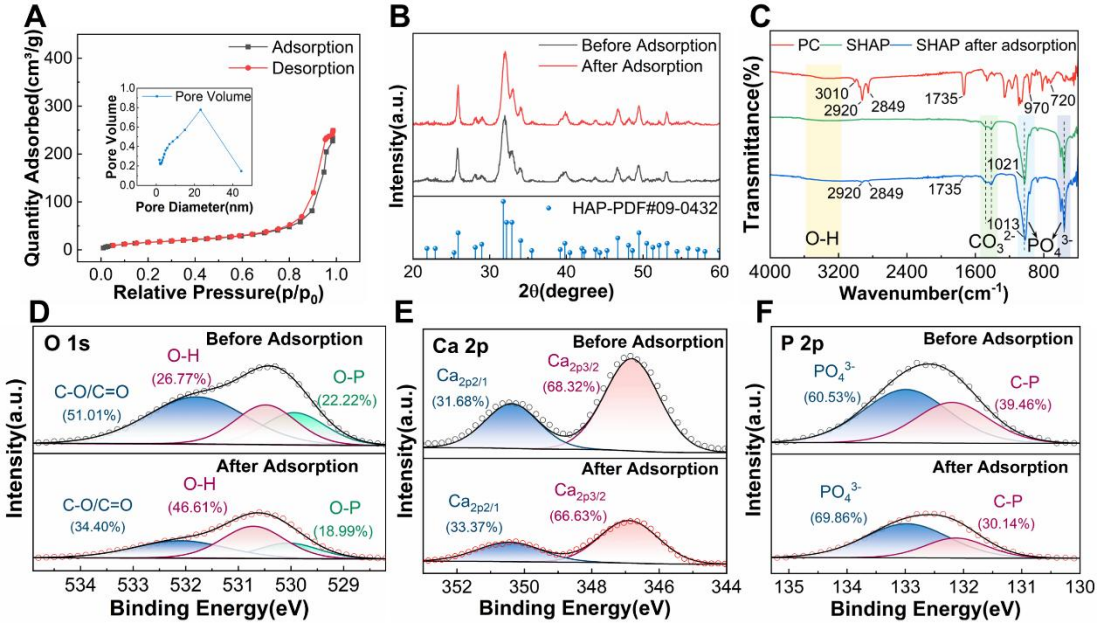

Fig. 5 Spectroscopic and textural characterizations of SHAP before and after PC adsorption: (A) N_2 adsorption-desorption isotherms and pore-size distribution (inset); (B) XRD patterns; (C) FT-IR spectra. High-resolution XPS spectra: (D) O 1s, (E) Ca 2p, and (F) P 2p for SHAP before and after adsorption

XPS analysis was further conducted to investigate the surface chemical states of SHAP before and after adsorption. The emerging of N element in the XPS spectrum indicated the adsorption of PC (**Fig. S7**). The

high-resolution XPS spectra of O 1s, Ca 2p, and P 2p were analyzed to further elucidate the PC adsorption mechanism. As shown in **Fig. 5D**, the high-resolution O 1s spectrum was recorded and deconvoluted into three peaks. After adsorption, the relative contribution of the O-H component increased significantly, accompanied by a shift toward higher binding energy, demonstrating the involvement of hydrogen-bond interactions in the adsorption process (Bensalah et al., 2020). Furthermore, the intensity of the Ca 2p peak decreased after PC adsorption, and the shift of the XPS peak toward a higher binding energy indicates that Ca^{2+} was involved in chemical interactions with PC (**Fig. 5E**). The high-resolution P 2p spectrum showed that the proportion of PO_4^{3-} increased significantly from 60.53% before adsorption to 69.86% (**Fig. 5F**). Such variation originated from ligand exchange between PL headgroups and surface Ca^{2+}, perturbing the electronic environment of HAP surface phosphate groups and causing the P 2p peak to shift toward lower binding energy(Yi et al., 2026). Based on the above results, the specific adsorption of PC on the SHAP surface can be explained by the following mechanisms: (i) hydrogen bonding recognition between the hydroxyl groups on the SHAP surface and the polar headgroups of the PC, and (ii) ligand exchange between the phosphate groups of PC and surface Ca^{2+}, leading to chemical anchoring.

3.4. Condition optimization for PLs enrichment from AKO

To establish the practical application conditions for SHAP-based PLs enrichment from AKO, the effects of AKO proportion, adsorption time, and temperature were systematically evaluated. As shown in **Fig. 6A**, Q_a increased with increasing AKO proportion and reached a maximum at 30% AKO, after which it declined at higher proportions. At 30% AKO, the adsorbent sites were effectively utilized, whereas at excessively high AKO concentrations, the adsorption capacity decreased. This reduction was likely because PLs tended to

aggregate at high concentrations, which could block the surface-active mesopores and reduce the accessibility of adsorption sites (Lee et al., 2023). Therefore, 30% AKO was selected as the optimal proportion to balance adsorption capacity and substrate utilization. The effect of adsorption time on the enrichment of PLs was then investigated (**Fig. 6B**). The adsorption process reached equilibrium after about 25 min, with no significant further increase in adsorption capacity. This rapid equilibrium indicated that SHAP possessed abundant accessible adsorption sites and strong affinity toward PLs, allowing efficient enrichment within a short contact time. Thus, 25 min was chosen as the optimal adsorption time for practical operation. The influence of temperature on PLs adsorption was also evaluated (**Fig. 6C**). High temperatures were detrimental to adsorption, with Q_a decreasing as the temperature increased from 20°C to 60°C. This behavior was consistent with the exothermic nature of PC adsorption observed in the isotherm study (**Table 2**). Therefore, 20°C was selected as the optimal condition, which also reduced energy consumption for practical applications.

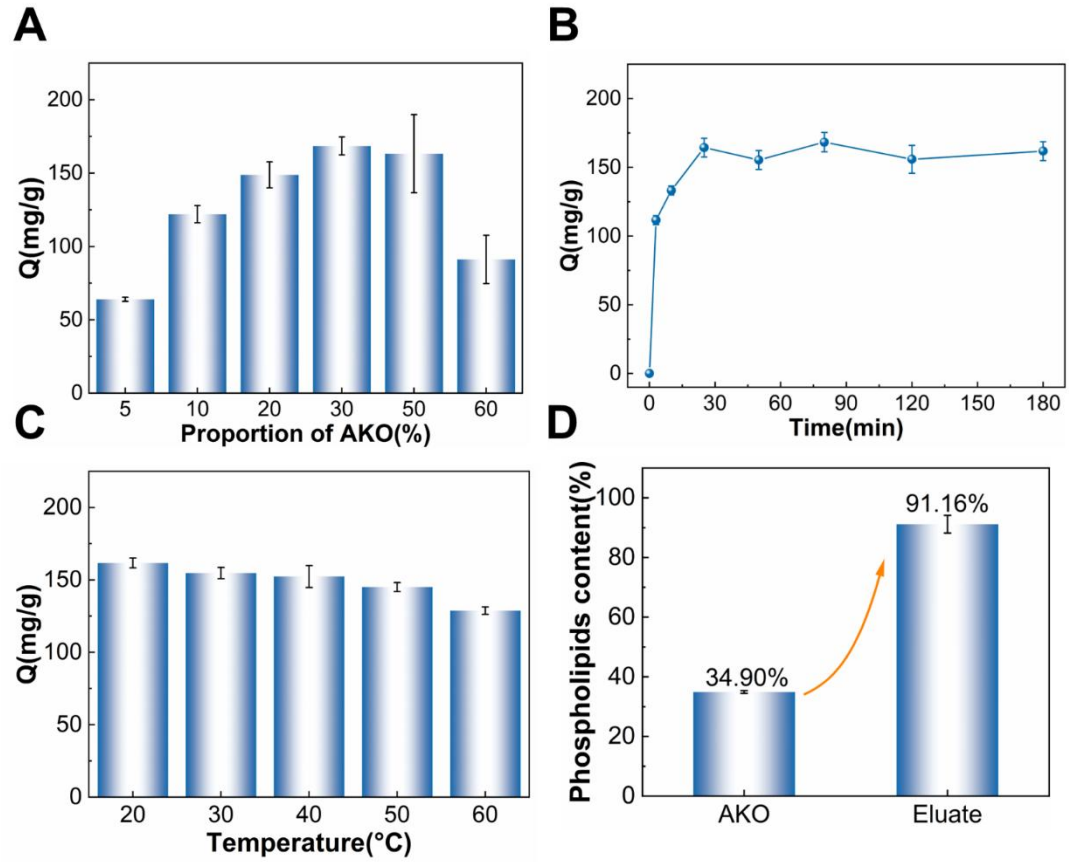

Fig. 6 Optimization of enrichment conditions for PLs from AKO using SHAP: influences of (A) AKO proportion, (B) adsorption time and (C) adsorption temperature. (D) PLs contents in raw AKO and the final eluted fraction after SHAP treatment

Under the optimized conditions (30% AKO, 25 min, 20°C), SHAP achieved an equilibrium adsorption capacity of 168.52±4.98 mg/g. This value was higher than that predicted by the PC isotherm, likely due to the presence of a broader spectrum of PL species in AKO, that may provide additional adsorption interactions. Moreover, the PL purity in the eluate increased from 34.90% in raw AKO to 91.16% after SHAP treatment **(Fig. 6D)**. The excellent enrichment performance of SHAP for in enriching high-value PLs from AKO made the SHAP-based strategy practical and efficient for AKO valorization.

4. CONCLUSION

In this study, mesoporous SHAP with typical hydroxyapatite crystal structure and high specific surface

area (124.60 m^2/g) was rapidly synthesized from calcined seashell powder under optimized conditions (Ca/P 2.19, pH 11.5, 350 W microwave for 3 min at 850 °C). The obtained SHAP exhibited prominent selectivity for PLs over TAG in complex AKO, with an adsorption capacity of 94.21±4.87 mg/g, 13.3 times that of triacylglycerols. PC adsorption on SHAP followed the pseudo-second-order kinetic and Langmuir isotherm models, indicating monolayer interfacial adsorption involving both physisorption and chemisorption. Thermodynamic parameters exhibited the adsorption of PC on SHAP was an exothermic process. FTIR, XRD, BET and XPS revealed that hydrogen-bonding and ligand-exchange between PL phosphate groups and surface Ca^{2+} sites synergistically drove PL selective recognition. Under the optimal conditions for enrichment PLs from AKO, SHAP reached a capacity of 168.52±4.98 mg/g within 25 min from 30 % AKO, enhancing the PL purity in eluate to 91.16% from 34.90% in raw AKO. Overall, by valorizing waste seashells into SHAP, this work not only provides an efficient and sustainable route for the selective enrichment of phospholipids from crude oils, but also unravels the adsorption behavior and mechanism of PC on hydroxyapatite surfaces, offering mechanistic guidance for the rational design of highly selective adsorbents and the scalable production of high-value phospholipid products.

Author Contributions Tong Jiang: Investigation, Visualization, Validation, Formal analysis, Data curation, Writing - original draft. Meilin Zhang: Visualization, Investigation, Data curation, Conceptualization. Yihong Chen: Methodology, Validation, Software. Jian'an Sun: Methodology, Supervision. Yang Hu: Conceptualization, Supervision, Project administration, Funding acquisition.

Funding This work was supported by National Key R&D Program of China (2024YFD2401604) and Young Talent of Lifting engineering for Science and Technology in Shandong，China (SDAST2025 QTA078).

Data Availability Data will be made available on request.

Declarations

Conflict of Interest The authors declare no competing interests.

REFERENCES

Alamdari, A., & Journey, Z. A. (2026). MOF-based strategies for bisphenol A remediation in water: From adsorption to photocatalytic degradation. *Journal of Hazardous Materials Advances*, *22*, 101211.

Amenaghawon, A. N., Anyalewechi, C. L., Darmokoesoemo, H., & Kusuma, H. S. (2022). Hydroxyapatite-based adsorbents: Applications in sequestering heavy metals and dyes. *Journal of Environmental Management*, *302*, 113989.

Bai, X., Lam, S. M., Nie, P., Xu, M., Liu, S., Shui, G., & Hu, G. (2022). Lipidomic analysis probes lipid coronas on hydrophilic nanoparticles from natural lung surfactant. *Environmental Science: Nano*, *9*(11), 4150–4161.

Balabadra, K. M., Panneer Selvam, S., Ramadoss, R., & Sundar, S. (2024). Hydroxyapatite synthesis and characterization from marine sources: A comparative study. *Journal of Oral Biology and Craniofacial Research*, *14*(6), 706–711.

Bar-On, Y. M., Phillips, R., & Milo, R. (2018). The biomass distribution on Earth. *Proceedings of the National Academy of Sciences*, *115*(25), 6506–6511.

Bensalah, H., Younssi, S. A., Ouammou, M., Gurlo, A., & Bekheet, M. F. (2020). Azo dye adsorption on an industrial waste-transformed hydroxyapatite adsorbent: Kinetics, isotherms, mechanism and regeneration studies. *Journal of Environmental Chemical Engineering*, *8*(3), 103807.

Calvano, C. D., Jensen, O. N., & Zambonin, C. G. (2009). Selective extraction of phospholipids from dairy products by micro-solid phase extraction based on titanium dioxide microcolumns followed by MALDI-TOF-MS analysis. *Analytical and Bioanalytical Chemistry*, *394*(5), 1453–1461.

Cotmore, J. M., Nichols, G., & Wuthier, R. E. (1971). Phospholipid-Calcium Phosphate Complex: Enhanced Calcium Migration in the Presence of Phosphate. *Science*, *172*(3990), 1339–1341.

Cui, X.-Y., Jiang, S., Wang, C.-C., Yang, J.-Y., Zhao, Y.-C., Xue, C.-H., Wang, Y.-M., & Zhang, T.-T. (2022). Comparative Analyses of EPA-Phosphatidylcholine, EPA- Lysophosphatidylcholine, and DHA-Lysophosphatidylcholine on DHA and EPA in n-3 PUFA-Deficient Mice. *Journal of Agricultural and Food Chemistry*, *70*(41), 13327–13339.

Delfanian, M., & Azizi, M. H. (2026). Complex coacervation of pea/soy protein, pectin and OSA-modified starch as carriers for EPA/DHA in soy milk-effervescent tablets: Simulated digestion and sensory attributes. *International Journal of Biological Macromolecules*, *364*, 152257.

Fitriyana, D. F., Ismail, R., Bayuseno, A. P., Widodo, R. D., Rusiyanto, R., Anis, S., Siregar, J. P., & Cionita, T. (2024). Synthesis of hydroxyapatite from biological sources prepared by the microwave irradiation method: A review. *Engineering Letters*, *32*(10), 1870–1881.

Frasnelli, M., Cristofaro, F., Sglavo, V. M., Dirè, S., Callone, E., Ceccato, R., Bruni, G., Cornaglia, A. I., & Visai, L. (2017). Synthesis and characterization of strontium-substituted hydroxyapatite nanoparticles for

bone regeneration. *Materials Science and Engineering: C*, *71*, 653–662.

Gao, K., Huang, W.-C., Dong, H., Sun, J., Jiang, H., & Mao, X. (2024). Engineering pickering emulsion with cell surface-displayed Esterase Est7 for specific and efficient synthesis of EPA monoglyceride. *Acs Sustainable Chemistry & Engineering*, *12*(21), 8061–8069.

Gu, G., Bai, Y., Chen, M., Du, J., Liu, B., Zhang, M., Yang, W., & Shao, Z. (2025). Template synthesis of CoFe-modified TiO_2 for highly selective enrichment of phosphatides. *Microchemical Journal*, *212*, 113300.

Gudyka, J., Ceja-Vega, J., Ivanchenko, K., Morocho, Z., Panella, M., Gamez Hernandez, A., Clarke, C., Perez, E., Silverberg, S., & Lee, S. (2024). Concentration-Dependent Effects of Curcumin on Membrane Permeability and Structure. *ACS Pharmacology & Translational Science*, *7*(5), 1546–1556.

Han, Q., Zhang, H., Sun, J., Liu, Z., Huang, W., Xue, C., & Mao, X. (2019). Immobilization of phospholipase D on silica-coated magnetic nanoparticles for the synthesis of functional phosphatidylserine. *Catalysts*, *9*(4), 361.

Heyen, S., Schneider, V., Hueppe, L., Meyer, B., & Wilkes, H. (2023). Variations of intact phospholipid compositions in the digestive system of Antarctic krill, Euphausia superba, between summer and autumn. *PLoS ONE*, *18*(12), e0295677.

Janusz, W., & Skwarek, E. (2022). Adsorption of malic acid at the hydroxyapatite/aqueous NaCl solution interface. *Applied Nanoscience*, *12*(4), 1355–1363.

Jiang, J., Long, Y., Hu, X., Hu, J., Zhu, M., & Zhou, S. (2020). A facile microwave-assisted synthesis of mesoporous hydroxyapatite as an efficient adsorbent for Pb^{2+} adsorption. *Journal of Solid State Chemistry*, *289*, 121491.

492 Jiang, X., Liu, Z., Yan, B., Zhao, L., Chen, T., & Yang, X. (2024). Effects of active silicon amendment on
493 Pb(II)/Cd(II) adsorption: Performance evaluation and mechanism. *Journal of Hazardous Materials*, *478*,
494 135614.
495 Lee, B.-M., Moon, W., Baek, K., Park, K.-H., Chung, S. H., & Chung, G. (2023). Ultraviolet irradiation
496 confers titanium oxide oleophilicity. *Journal of Materials Science*, *58*(12), 5258–5268.
497 Li, D., Zhang, Z.-T., He, C.-W., & Xie, Z. (2021). Yeast Lipid Extraction and Analysis by HPTLC. *Bio-*
498 *Protocol*, *11*(13), e4081.
499 Li, Y., & Liu, G. (2024). Encapsulation of Antarctic krill oil and kaempferol co-loaded nano-liposomes in
500 alginate-chitosan hydrogel beads: Improved stability and modified digestive behaviour. *International Journal*
501 *of Food Science & Technology*, *59*(5), 3198–3211.
502 Liu, D., Lipponen, K., Quan, P., Wan, X., Zhan, H., Makila, E., Salonen, J., Kostiainen, R., Hirvonen, J.,
503 Kotiaho, T., & Santos, H. A. (2018). Impact of pore size and surface chemistry of porous silicon particles and
504 structure of phospholipids on their interactions. *Acs Biomaterials Science & Engineering*, *4*(7), 2308–2313.
505 Liu, Y., Shan, L., & Wang, X. (2009). Purification of soybean phosphatidylcholine using D113-III ion
506 exchange macroporous resin packed column chromatography. *Journal of the American Oil Chemists Society*,
507 *86*(2), 183–188.
508 Lu, L., Li, C., Tai, H., Zhang, H., Huang, Z., Ke, L., Liang, Y., Ma, F., Shang, J. K., & Li, Q. (2026). Effective
509 removal of Cs^+ from a model polar organic medium by a magnetically separable adsorbent. *Separation and*
510 *Purification Technology*, *416*, 140058.
511 Ma, X., Wang, L., He, Q., Sun, Q., Yin, D., & Zhang, Y. (2023). A review on recent developments and

applications of green sorbents-based solid phase extraction techniques. *Advances in Sample Preparation*, *6*, 100065.

Manyepedza, T., Gaolefufa, E., Koodirile, G., Beas, I. N., Gorimbo, J., Modukanele, B., & Kabomo, M. T. (2025). Sustainable adsorbents for wastewater treatment: Template-free mesoporous silica from coal fly ash. *Chemical Engineering & Technology*, *48*(7), e70077.

Martínez Pérez-Cejuela, H., Ten-Doménech, I., El Haskouri, J., Amorós, P., Simó-Alfonso, E. F., & Herrero-Martínez, J. M. (2018). Solid-phase extraction of phospholipids using mesoporous silica nanoparticles: Application to human milk samples. *Analytical and Bioanalytical Chemistry*, *410*(20), 4847–4854.

Mondal, S., Hoang, G., Manivasagan, P., Moorthy, M. S., Vy Phan, T. T., Kim, H. H., Nguyen, T. P., & Oh, J. (2019). Rapid microwave-assisted synthesis of gold loaded hydroxyapatite collagen nano-bio materials for drug delivery and tissue engineering application. *Ceramics International*, *45*(3), 2977–2988.

Nga, N. K., Thuy Chau, N. T., & Viet, P. H. (2018). Facile synthesis of hydroxyapatite nanoparticles mimicking biological apatite from eggshells for bone-tissue engineering. *Colloids and Surfaces B: Biointerfaces*, *172*, 769–778.

Phleger, C. F., Nelson, M. M., Mooney, B. D., & Nichols, P. D. (2002). Interannual and between species comparison of the lipids, fatty acids and sterols of Antarctic krill from the US AMLR Elephant Island survey area. *Comparative Biochemistry and Physiology B-Biochemistry & Molecular Biology*, *131*(4), 733–747.

Pinto, G., Caira, S., Mamone, G., Ferranti, P., Addeo, F., & Picariello, G. (2014). Fractionation of complex lipid mixtures by hydroxyapatite chromatography for lipidomic purposes. *Journal of Chromatography A*, *1360*, 82–92.

Pusparizkita, Y. M., Faizal, R. A., Negara, S. A. P., Ismail, R., Jamari, J., & Bayuseno, A. P. (2025). A microwave-assisted hydrothermal method for rapidly synthesizing nanocrystalline carbonated hydroxyapatite from calcium resources in crab shell waste. *Next Materials*, *9*, 100946.

Sadat-Shojai, M., Kalantari-Lalari, M., & Asadnia, M. (2023). Synthesis of highly regular dandelion-like hydroxyapatite particles-a Taguchi experimental design approach. *Crystengcomm*, *25*(24), 3564–3575.

Shen, Q., Yang, M., Li, L., & Cheung, H.-Y. (2014). Graphene/TiO_2 nanocomposite based solid-phase extraction and matrix-assisted laser desorption/ionization time-of-flight mass spectrometry for lipidomic profiling of avocado (Persea americana Mill.). *Analytica Chimica Acta*, *852*, 153–161.

Stewart, J. C. M. (1980). Colorimetric determination of phospholipids with ammonium ferrothiocyanate. *Analytical Biochemistry*, *104*(1), 10–14.

Takeda, H., Takeuchi, M., Hasegawa, M., Miyamoto, J., & Tsugawa, H. (2024). A Procedure for Solid-Phase Extractions Using Metal-Oxide-Coated Silica Column in Lipidomics. *Analytical Chemistry*, *96*(43), 17065–17070.

Wang, D., Kang, L., Hamdi, M., Shen, X., Li, S., Lu, L., & Su, F. (2025). Advanced ultrasounds-assisted natural deep eutectic solvents green strategy for the sustainable extraction of biocompatible nano-hydroxyapatite from fish scales. *Journal of Molecular Liquids*, *428*, 127515.

Wang, M., Zhang, F., Debrah, A. A., Khan, J., Hou, H., Yuan, Q., & Du, Z. (2023). Selective extraction of phospholipids from human milk using glass fabric modified with zirconium-based metal organic framework. *Journal of Chromatography A*, *1710*, 464435.

Wende, L. M., Carpanedo, L., Scholz, L., Kampschulte, N., West, A. L., Calder, P. C., & Schebb, N. H. (2026).

552 Quantification of esterified oxylipins following HILIC-fractionation of lipid classes. *Journal of Lipid*
553 *Research*, *67*(1), 100950.

554 Wu, L. N. Y., Genge, B. R., & Wuthier, R. E. (2009). Differential effects of zinc and magnesium ions on
555 mineralization activity of phosphatidylserine calcium phosphate complexes. *Journal of Inorganic*
556 *Biochemistry*, *103*(7), 948–962.

557 Wu, S.-C., Hsu, H.-C., Ji, H.-Y., & Ho, W.-F. (2024). Comparative Study of Cu Ion Adsorption by Nano-
558 Hydroxyapatite Powder Synthesized from Chemical Reagents and Clam Shell-Derived Calcium Sources.
559 *Nanomaterials*, *14*(17), 1431.

560 Yi, C., Li, S., Bai, Z., Lu, A., He, G., Zhou, J., & Wei, Y. (2026). Three-dimensional porous nano-
561 hydroxyapatite@gelatin composite as efficient adsorbent for uranyl ion removal from low-level radioactive
562 wastewater. *Journal of Environmental Sciences*, *168*, 413–422.

563 Yu, H.-Y., Park, S.-E., Chun, H. S., Rho, J.-R., & Ahn, S. (2022). Phospholipid composition analysis of krill
564 oil through HPLC with ELSD: Development, validation, and comparison with 31P NMR spectroscopy.
565 *Journal of Food Composition and Analysis*, *107*, 104408.

566 Zhou, L., Wu, X., Yang, F., Zhang, M., Huang, R., & Liu, J. (2021). Characterization of molecular species
567 and anti-inflammatory activity of purified phospholipids from Antarctic krill oil. *Marine Drugs*, *19*(3), 124.

568 Zhu, Z., Yang, Y., Fan, Y., Zhang, L., Tang, S., Zhu, Y., & Zhou, X. (2022). Strontium-doped hydroxyapatite
569 as an efficient adsorbent for Cd(II) removal from wastewater: Performance, kinetics, and mechanism.
570 *Environmental Technology & Innovation*, *28*, 102575.

571 Zou, Y., Diao, D., Zhang, H., Qiu, Z., Wang, Y., Qian, Z., Ding, H., Yang, J., & Xiao, X. (2025). Evaluation

of the efficient fluoride removal of porous CeO_2/HAP: Performance and mechanism study. *Separation and Purification Technology*, *364*, 132527.

Supplementary Files

This is a list of supplementary files associated with this preprint. Click to download.

- Supplementarymaterial.docx